EUROPEAN ORGANIZATION FOR NUCLEAR RESEARCH

CERN–ECP/96–12
10 October 1996

TIME STABILITY OF ASYMMETRIC FABRY-PEROT MODULATOR BASED ANALOG LIGHTWAVE LINKS

G. Cervelli, R. Grabit, M. Persello, G. Stefanini, F. Vasey
CERN, Geneva, Switzerland

Abstract

Lightwave links for analog signal transfer are being developed and evaluated for application in high-density interconnects. The reflective links are based on compact electro-optic intensity modulators connected by ribbons of single-mode fibres to remotely located transceivers (lasers and photoreceivers) and read-out electronics. For long-term characterization, four Asymmetric Fabry-Perot Modulator (AFPM) prototypes were continuously operated and monitored over a period of eight months. The collected data allow evaluation of the system time stability and simulation of the possible recalibration procedures. The recalibration requirements to achieve the desirable accuracy and reliability are inferred statistically.

(Submitted to IEEE Journal of Lightwave Technology)

1. INTRODUCTION

Optical links find extensive use whenever the requirements on bandwidth, power dissipation and material budget become too demanding for conventional copper cabling. In preparation for the next generation of colliding beam experiments at the CERN Large Hadron Collider (LHC), high density optical interconnections are being developed for analog or digital signal transfer between the detector front-end electronics and the remote data-acquisition systems. Electro-optical transmitters will be mounted inside the detector volume and connected by optical fibres to remotely located receivers. In the CMS experiment [1], a 50 000-channel, 100-m-long, analog optical link will be used to transfer raw data at a rate of 40 million samples per second from the 15 million channels of the tracker detectors. Building such an optical link presents many challenges [2]. Key issues will be the long-term system reliability and time stability.

This paper addresses the time stability issue: a realistic link prototype has been monitored over a period of more than 5500 h under varying operational conditions. The optical link under test is based on external modulation of a laser beam using an electro-optical intensity modulator [3]. The Asymmetric Fabry Perot Modulator (AFPM), a vertical InGaAs/InP multi-quantum-well (MQW) cavity, is operated in reflection mode; it is described in [4]. The measurements are performed on four-channel links using monolithic modulator arrays packaged in a compact housing [5]. The general measurement set-up is described in Section 2. The resulting experimental database serves as a rich template of system responses, which can be used both for characterization and for simulation purposes. Results are visualized in a compact and intuitive form, as defined in Section 3. The intrinsic performances of the evaluated channels are compared and their correlation with environmental parameters is studied in Section 4. Finally, a statistical method to quantify the time stability of the link performance is proposed in Section 5. It is used to simulate, evaluate and optimize possible recalibration procedures.

2. EXPERIMENTAL SET-UP AND MEASUREMENTS

The measurement set-up is shown in Fig. 1. Two system parts can easily be distinguished: the front-end electro-optical interface (modulators) and the back-end opto-electrical interface (transceiver module and laser source). The CW laser serving the four modulator channels is a high-power Fabry-Perot device. The wavelength of operation is 1.55 μm. The transceiver module performs all opto-electrical conversion functions on the back-end of the link. It fans out the DC optical power and sends it to the modulators across four optical channels. It detects and amplifies the back-reflected analog signals through four DC-coupled photoreceivers. The amplification is performed using low-noise transimpedance amplifiers followed by a differential gain stage featuring an overall differential transresistance of $R \approx 700$ kΩ and an equivalent current input noise of $I_n \approx 2.5$ pA/√Hz. The photodiodes are low back-reflection devices in order to reduce phase-to-intensity optical noise conversion in the link.

A controller kept both the laser drive-current and the laser temperature constant, so that both emitted light intensity and wavelength were expected to be stable. Nevertheless, the light intensity incident on the modulators was not stable; it was correlated with control room temperature, because of temperature sensitivity of the optical splitter and couplers spliced in series. A digital-to-analog converter set and swept the reverse bias at the modulators, while a data-logger read and stored the current through each modulator junction (via a 1-kΩ

resistance), as well as the output voltages of the photoreceivers. All these operations were coordinated by a central processor running LabVIEW software.

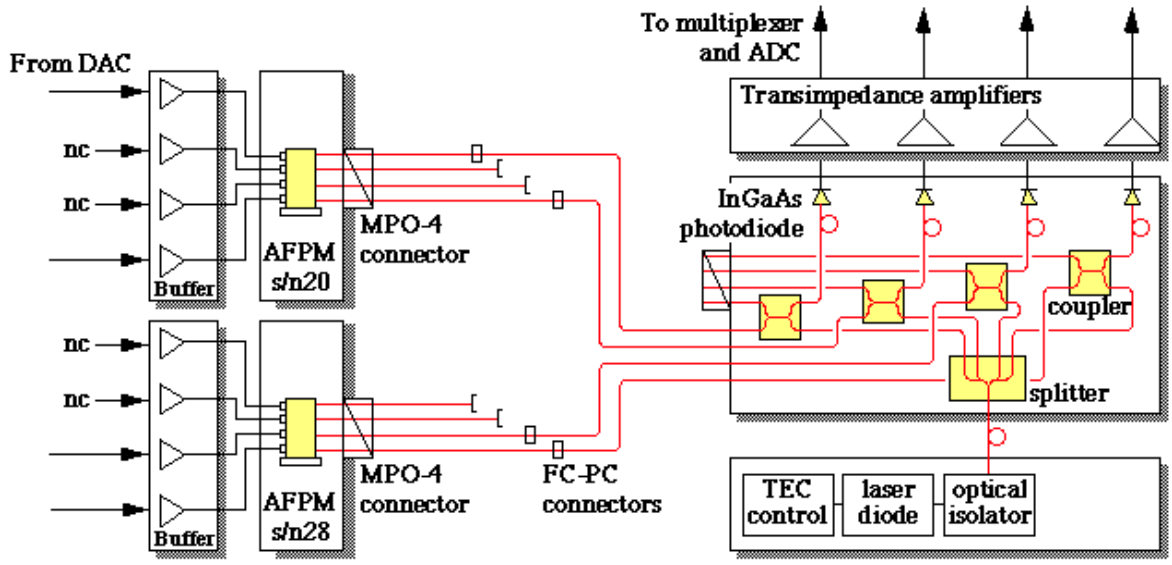

Figure 1: Experimental set-up. The transceiver module (on the right) consists of an FP laser diode, a 1×4 splitter, four 2×2 directional couplers, and four photoreceivers. The front-end module (on the left) contains two four-channel modulator chips (s.n.20 and s.n.28). Two channels were monitored in each chip, giving a total of four evaluated channels.

The reflectivity and absorption characteristics of the modulators were monitored through periodic measurement of the link input characteristics and transcharacteristics (see Fig. 2), both with the laser on and with the laser off. The *input characteristic* is defined as the current–voltage characteristic of the AFPM. When the laser was off, the measured current was simply the leakage current of the AFPM junction (or dark current). When the laser was on, a photo-generated current was added to the dark current in proportion to the absorbed optical power. This is called the *photocurrent characteristic* and was calculated as the difference between the total input current and the dark current. The *transcharacteristic* is the system response, i.e. the transceiver output voltage as a function of the modulator input-voltage. When the laser was off, there was no coupling between the input and the output of the link, and the measured output was constant and equal to the voltage offset given by the receiver. When the laser was on, the measured voltage was linearly dependent on the reflected power and thus on the modulator input-bias. The characteristics were sampled over a wide input range, centred around the linear region of the modulators. The input bias was reduced in regular steps from –5 to –15 V, as shown in Fig. 2.

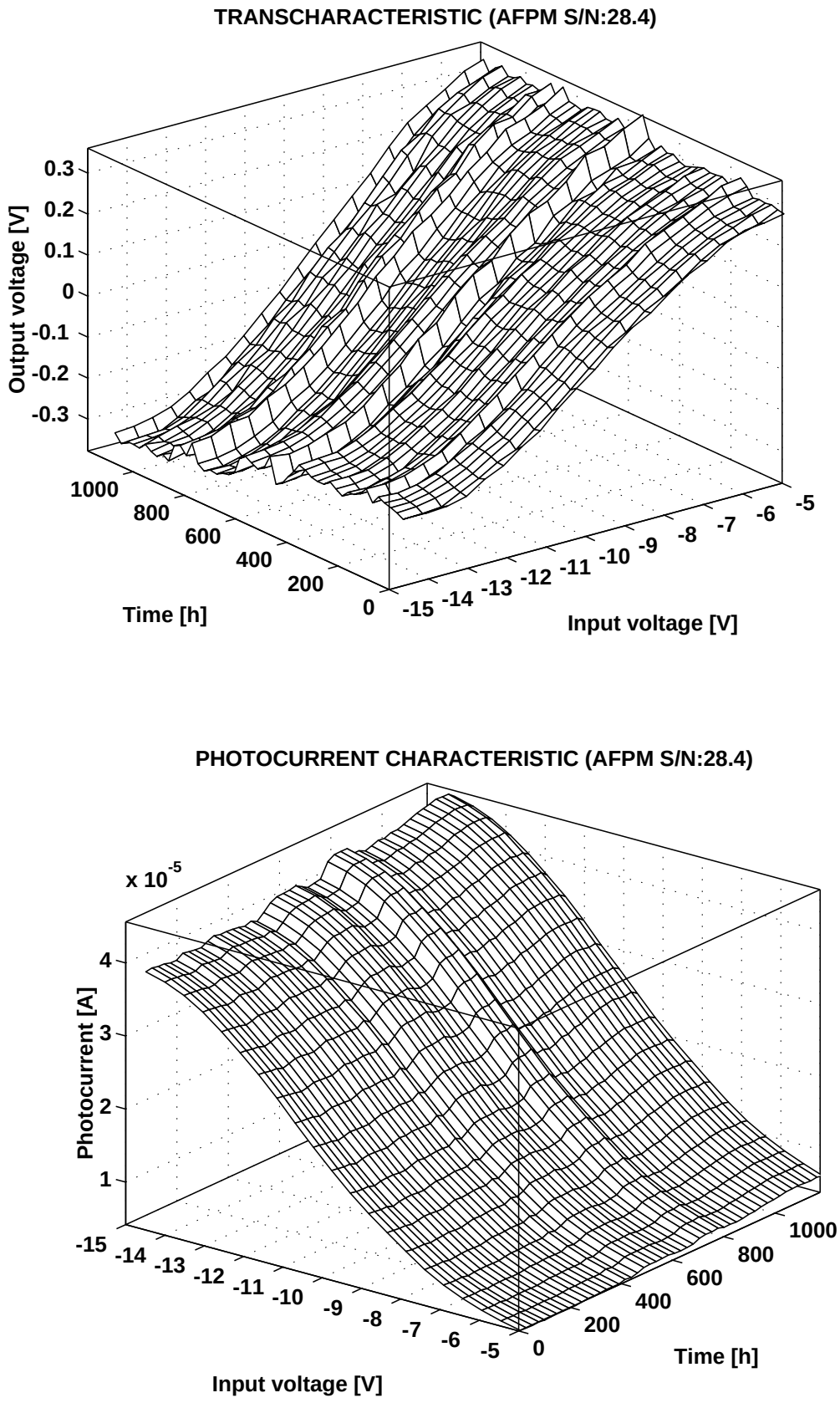

Figure 2: Transcharacteristic (top) and photocurrent characteristic (bottom) as a function of time, for a typical channel. Measurements were performed periodically, up to three times per hour.

The characteristics were measured over a period of 5539 h (almost eight months). A small amount of data was lost because of data acquisition interruptions due to software errors or upgrades. The periodicity of the measurements was initially set at 1 h. At time t = 3454 h some important software improvements were implemented. After that time: the input voltage was scanned with a dual resolution (0.5 and 0.2 V) for finer resolution around the linear region; each measurement was the result of an average of 10 acquisitions in quick succession (denoising); the measurement periodicity was decreased from 1 h to 20 min, allowing changes to be monitored with an improved time resolution; the temperature of the back-end electronics was monitored.

A template of almost 10 000 transcharacteristics, input characteristics and photocurrent characteristics per channel was obtained. This represents an empirical but realistic model of the system under varying environmental conditions. Figure 3 shows the temperature evolution during the whole period: diurnal oscillation in addition to seasonal trends are apparent.

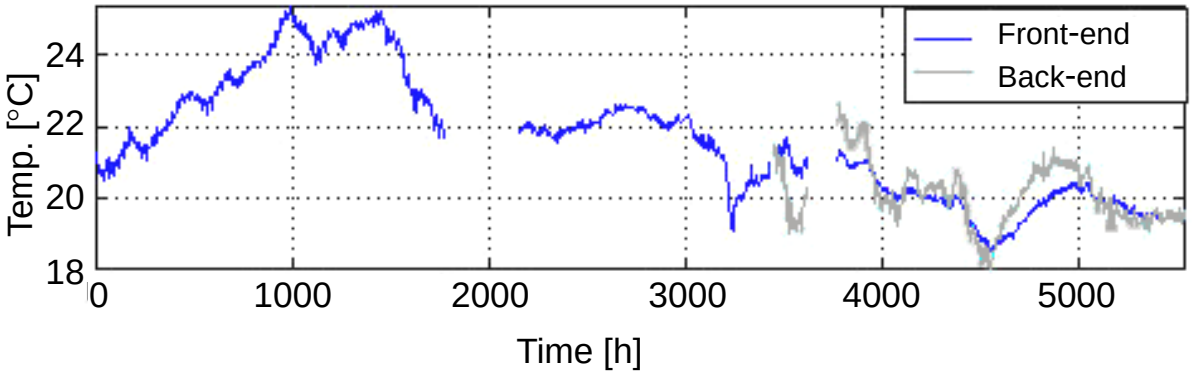

Figure 3: Temperature evolution during the experiment.

The collected data has been used both for performance and time stability characterization and for simulation of different recalibration procedures. The heavy data-analysis workload was eased by a more compact representation of the results, as discussed in the following section.

3. EVALUATION CRITERIA

The analog link response (transcharacteristic, input characteristic and photocurrent characteristic) can be written in the form $Y = f(X) + n(X)$, where X is the input signal, $f(X)$ is a deterministic function describing the average static characteristic response of the system, and $n(X)$ is a centred noise whose stochastic properties may depend on X. For characterization purposes, it is useful to evaluate the *linearity* and *modulation depth* of the deterministic part of the link response.

For analysis purposes, the response $f(X)$ was modelled as a sixth order polynomial fit of the measurement point, as shown in Fig. 4. In an ideal operational mode of the link, it is desirable that the response $f(X)$ is a linear function of the input X, so that the value of X can be determined precisely from the measurement of $f(X)$. However, in reality, this is true only within a certain approximation and only for a given range of input values (see Fig. 4). Based on a linear approximation

$$f(X) \approx Y_{\text{lin}} = Y_0 + G \cdot (X - X_0) \tag{1}$$

the real value of X is estimated (X_{est}) from

$$X_{\text{est}} = \frac{f(X) - Y_0}{G} + X_0 \quad . \tag{2}$$

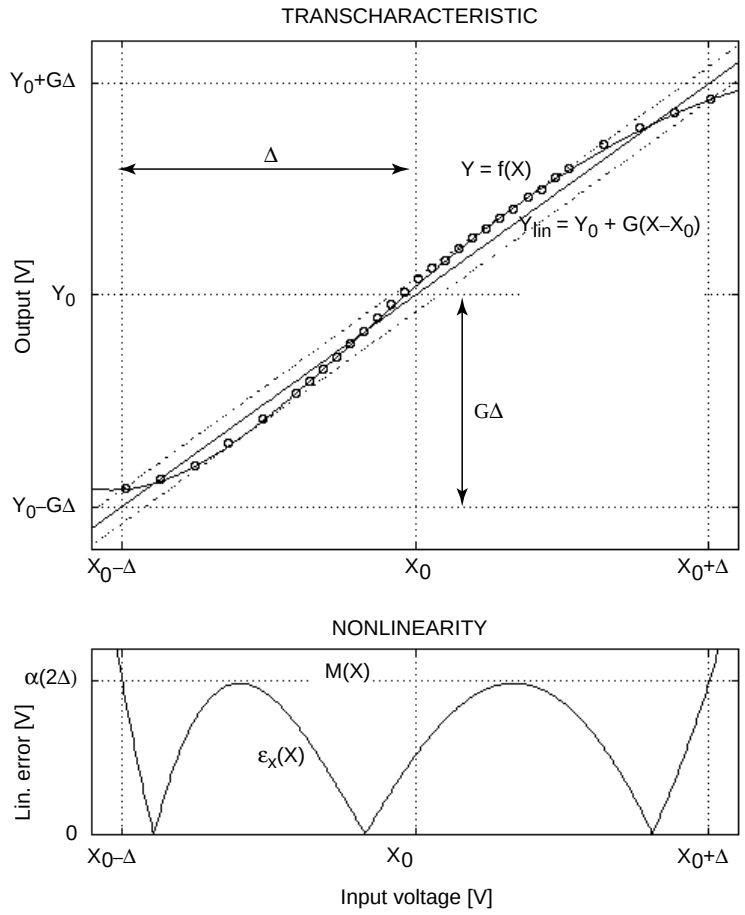

Figure 4: Definition of the link optimization criteria. The linearity error is the absolute deviation between the link response and its linear fit. The integral nonlinearity (α) is the maximum linearity error inside the nominal linear range, normalized to the linear range width ($2 \cdot \Delta$). An integral nonlinearity constraint α defines the linear input range Δ, for a given fit G. The optimization procedure maximizes the modulation depth ($G \cdot \Delta$) for a given α.

The error due to deviation from linearity (or *linearity error*) is

$$\varepsilon_x(X) = \left| X_{\text{est}} - X \right| = \left| \frac{f(X) - Y_0}{G} + X_0 - X \right| \tag{3}$$

and the input range of X must be restricted to a region where the characteristic function $f(X)$ has a linearity error $e_x(X)$ which is within a predefined maximum allowed error $M(X)$. This region is the *linear input range* and its linear transformation is the *linear output range*. The maximum allowed error $M(X)$ is a positive function defined arbitrarily according to the application anticipated for the system — it is dependent, among other things, on the nature of the signal (unipolar or bipolar), and the required precision (absolute or relative).

The compact representation of the characteristic is based on the following set of parameters (see Fig. 4): X_o, Y_o, G, and Δ. The first three parameters define the linear fit: $Y_{lin} = Y_o + G\cdot(X - X_o)$, where (X_o, Y_o) is a point on the fit line — not necessarily on the curve $f(X)$ — and G is the fit slope. X_o and Y_o are also the centres of the linear input range and linear output range, respectively, i.e. the intervals where the linearity conditions are met. The amplitudes of these intervals are defined by the specification of the fourth parameter Δ. The linear input range is thus $[X_o - \Delta, X_o + \Delta]$, and the linear output range is $[Y_o - G\cdot\Delta, Y_o + G\cdot\Delta]$. The term $G\cdot\Delta$ is the *modulation depth* and defines a quality factor of the link. The 'optimum' linear fit is defined by the maximization of this parameter for a given characteristic $f(X)$ and a given $M(X)$.

Procedures have been developed to evaluate the optimum linear fit to any characteristic in the general case. For long-term characterization purposes the computational load was too great and so was reduced by proposing the following two hypotheses: (a) the characteristics are assumed to be S-shaped (similar to the curve plotted in Fig. 4) and to have a dominant *cubic* component; (b) the acceptable error mask is defined to be uniform and proportional to the linear range width: $M(X) = \alpha\cdot(2\cdot\Delta)$, with $\alpha << 1$ (see Fig. 4). The maximum linearity error $\varepsilon_x(X)$ allowed over the linear input range, normalized to the input range width $(2\cdot\Delta)$, is called the *integral nonlinearity*. According to hypothesis (b) the integral nonlinearity must be less than or equal to α. Therefore,

$$\frac{\varepsilon_X(X)}{2\cdot\Delta} \le \alpha, \quad \forall X \in [X_0 - \Delta, X_0 + \Delta]. \tag{4}$$

Within the two hypotheses stated above, the linear fit to a characteristic is 'optimum' (i.e. it maximizes the modulation depth $G\cdot\Delta$) if and only if the corresponding integral nonlinearity is equal to α. The optimum linear fit is calculated using an iterative procedure. First the optimum linear fit to the cubic approximation of the characteristic is calculated analytically. This is an approximate solution, which is used as the iteration starting-point. The following steps converge it towards the actual solution. This simplified method of calculation gave excellent results. The convergence was fast and in most cases the solution could be determined with any desired degree of precision. The residual uncertainty, due to the noise term $n(X)$ affecting the raw data, has also been calculated and appears as *error bars* on the graphs in Fig. 5. It should be noted that the adopted method is purely morphological, and avoids any differential operation, thus limiting numerical errors. Evaluation of the system parameters as a function of time, provides a powerful means to quantify time stability and environmental-parameter dependence.

4. CHARACTERIZATION

Figures 3, 5, and 6 show the environmental parameters (temperature) and the processed results for the photocurrent characteristic and system transcharacteristic. The four monitored channels correspond to two modulator packages: s.n.20 and s.n.28. From the beginning of the experiment, the two channels corresponding to the first package (s.n.20.1 and s.n.20.4) showed a higher output noise because of a bad optical interface in the package. This resulted in the instability of the parameters with time, which is particularly visible in the reflectivity plots (Fig. 6).

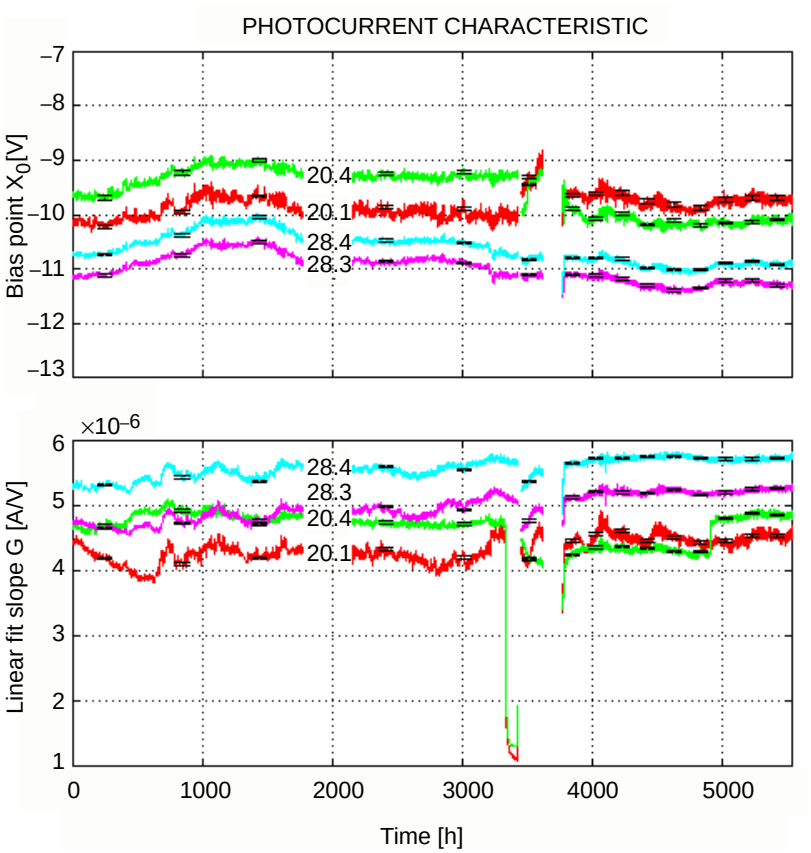

Figure 5: Calculated linear-fit parameters of the photocurrent characteristic.

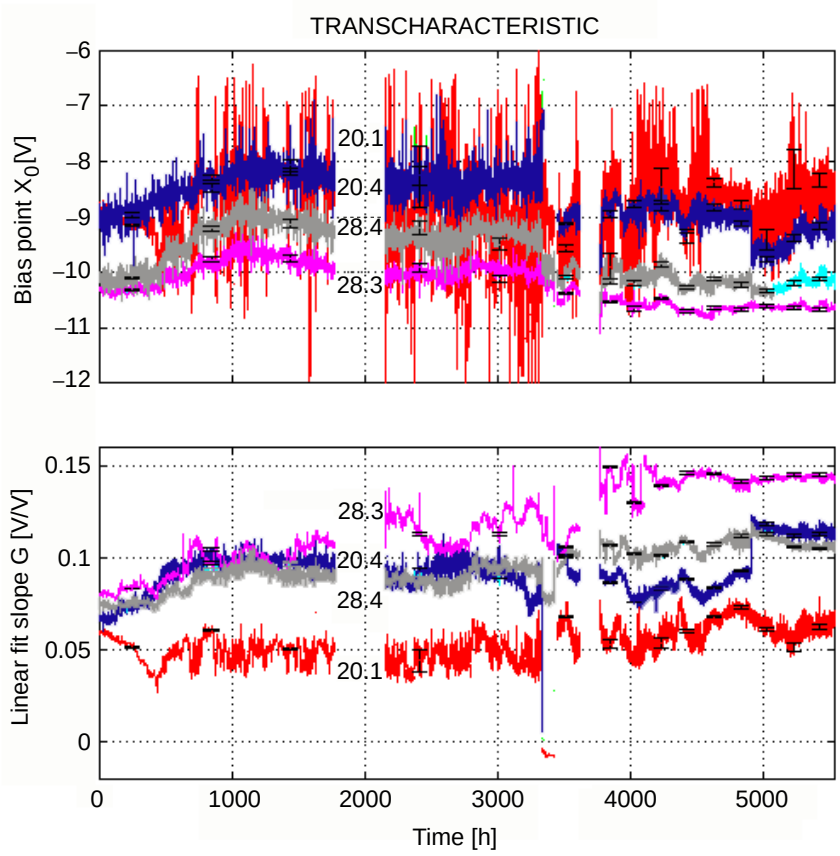

Figure 6: Calculated linear-fit parameters of the transcharacteristic.

The dark current of the s.n.28 assembly increased by several orders of magnitude during monitoring. This showed very little correlation with environmental parameters, and was attributed to the formation of parasitic leakage channels along the passivation layers of the AFPM junction [6]. However, dark current variations do not directly affect the absorption–reflectivity properties of the voltage-driven modulator, and therefore do not affect either the photocurrent characteristic (photo-generated portion of the total leakage current), which is proportional to the absorbed power, or the transcharacteristic, which is proportional to the reflected power.

The photocurrent characteristic (Fig. 5) represents an image of the modulators only, and depends on environmental parameters through the incident power, fibre coupling (package) and die behaviour, whereas the transcharacteristic (Fig. 6) describes the behaviour of the full link, and so is also dependent on the transceiver optics and electronics. Therefore, the relative influence of various environmental factors on the system transcharacteristic is more difficult to determine. By comparing Figs. 5 and 6, it is clear that the global system response (Fig. 6) was much more unstable and noisier than the photocurrent (Fig. 5). Correlation plots for the first 1000 h of observation (Fig. 7) confirmed a very clear dependence of the modulator photocurrent bias-point on the irradiation-cell temperature, which was not immediately visible on the reflectivity plots. The correlation is due to the temperature dependence of the MQW exciton peak position. The measured positive shift was of the order of 0.15 V/°C (see Fig. 7).

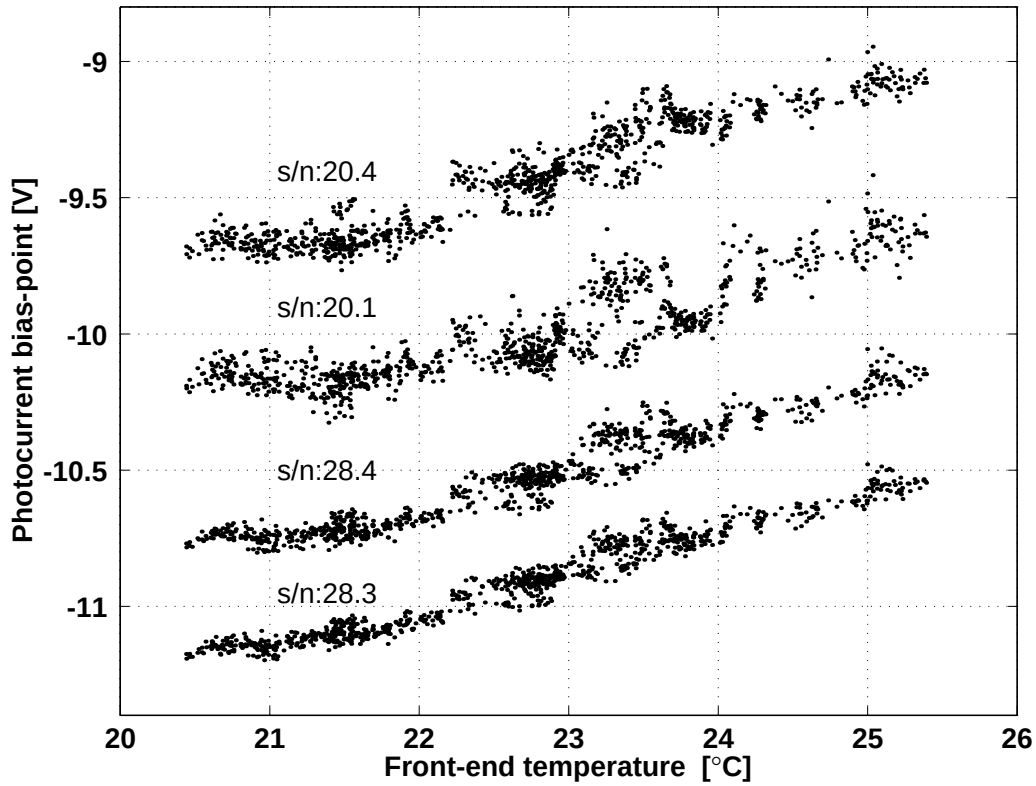

Figure 7: Correlation between photocurrent bias-point and front-end temperature, showing a linear temperature dependence ($dX_o/dT \approx 0.15$ V/°C).

The linearity centre (X_o) of the photocurrent plots (Fig. 5) was systematically 0.5 to 1 V different from that of the reflectivity plots (Fig. 6). This was confirmed by independent

laboratory measurements. The width of the linear region $2 \cdot \Delta$ (relative to an integral nonlinearity of $\alpha = 1\%$) was in all cases larger than 3 V. It can be reduced if tighter integral-nonlinearity requirements need to be met.

A few computer-control errors occurred during the monitored period, and some data were lost. On one occasion (at time $t = 3454$ h) the laser temperature controller did not start correctly, and for some time the laser was left uncooled. Despite the poor quality of the corresponding data, this fact added new possibilities to the analysis, since it was then possible to observe the system response to a power (and wavelength) step, when the temperature control was turned on again ($t = 3783$ h). Figure 5 shows clearly that the bias-point shifted in correspondence with the laser temperature step. Independent measurements showed that this could not be a power effect. As it is the temperature of the laser diode which is varied, the wavelength of the emitted light is also changed. According to the laser data sheets, the temperature dependence of the wavelength for a Fabry-Perot laser (0.5 nm/°C) is high enough to explain the magnitude of the bias-point shift. Differences from channel to channel, visible in the plots, can be attributed to the uneven quality of the fibre butt-coupled interface. The requirement for a linear region stability within a few hundred millivolts translates into a requirement for a wavelength stability within a few angstroms.

5. TIME STABILITY AND PERIODIC RECALIBRATION

The set of collected data represents a comprehensive overview of the long-term link behaviour, subject to environmental parameter fluctuations. An empirical stability model can be inferred from these data, and realistic operation of the system can be simulated.

Despite the fact that in the final application the front-end temperature will be controlled, the time instability of the link behaviour is still a cause of concern, and some procedure for automatic recalibration must be foreseen. We use the collected data to analyse and quantify the performance degradation due to system instability. The effect of the recalibration period on the statistics of the integral nonlinearity is studied, and the recalibration time is optimized according to the application requirements.

The set of fit parameters X_o, Y_o, G, and Δ was defined in Section 3. These parameters can be optimized for a given characteristic $f(X)$ to maximize the modulation depth $G \cdot \Delta$, given an allowed integral nonlinearity α. If the parameters are optimized for the characteristic $f(X)$ at the observation time, the linearity error is lower than α for all values of X belonging to the linear region. However, because of time instabilities, a time-dependent component is added to the error and the integral nonlinearity quickly becomes greater than α. Periodic recalibration then becomes necessary, with a frequency determined according to the statistical distribution of the performance degradation.

Figure 8 shows an example of the integral-nonlinearity evolution soon after recalibration. The parameters are optimized at a time $t = t_o$ (set arbitrarily to 4000 h in the plot) for an integral nonlinearity of $\alpha = 1\%$. Because of transfer function instability, the integral nonlinearity for $t > t_o$ increases above the optimized value α (to 3% after only 25 h, to 6% after 400 h, etc.). The short-term performance degradation can be significant, thus justifying the need for periodic recalibration.

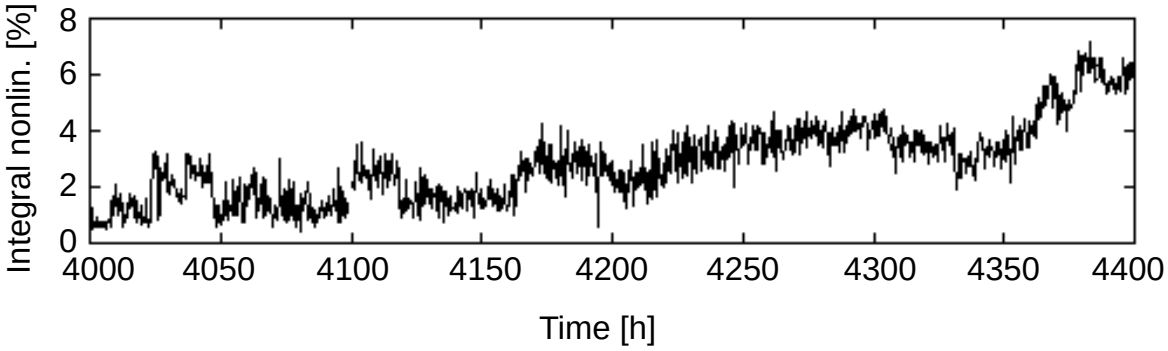

Figure 8: Integral-nonlinearity degradation due to the time instability of the system response (AFPM s.n.28.4) when no periodic recalibration is performed.

In the context of our simulation, the term 'recalibration' refers to the optimization of the linear-fit parameters (according to a given criterion) at a specific moment in time. This is an abstract operation performed mathematically assuming a precise knowledge of the system transfer function $f(X)$. No practical consideration about its implementation in a real system is given here.

To allow comparison between different channels to be made, the time stability must be calculated for equal performance in terms of linear range. The recalibration procedure therefore uses a fixed linear-range width of 3 V (Δ = 1.5 V), and the fit parameters X_o, Y_o, and G are optimized to give a minimum integral nonlinearity α within the interval $[X_o - \Delta, X_o + \Delta]$.

The analysis was performed on data collected from t = 3454 h to t = 5539 h, corresponding to high-resolution data (see Section 2). The s.n.20.1 modulator channel was not analysed since its data were too noisy and not considered to be representative of typical system behaviour.

The analysis was carried out following two different approaches. In the first approach, the maximum acceptable linearity error was fixed arbitrarily, as an upper threshold, and the recalibration was triggered whenever the actual maximum error passed this threshold. This method is noise limited. Recalibration was triggered almost continuously by noise spikes, and it was difficult to extract any useful information about the system performance in the operational region of interest (integral nonlinearity contained within a few percent). In the second approach, the recalibration period T_c was fixed, and the recalibration was performed at regular intervals. For each value of T_c, the linearity error statistics were studied. Figure 9 shows an example of this approach. The recalibration was simulated with a periodicity of 12 h. An output AC coupling was assumed, so that Y_o was always equal to zero. The other parameters (X_o and G) were constant in the time interval between two successive recalibrations, and were only updated when the recalibration took place. The evolution of the corresponding integral nonlinearity was monitored. It periodically started from a minimum at the recalibration time, and deviated randomly during the time interval between two successive recalibrations.

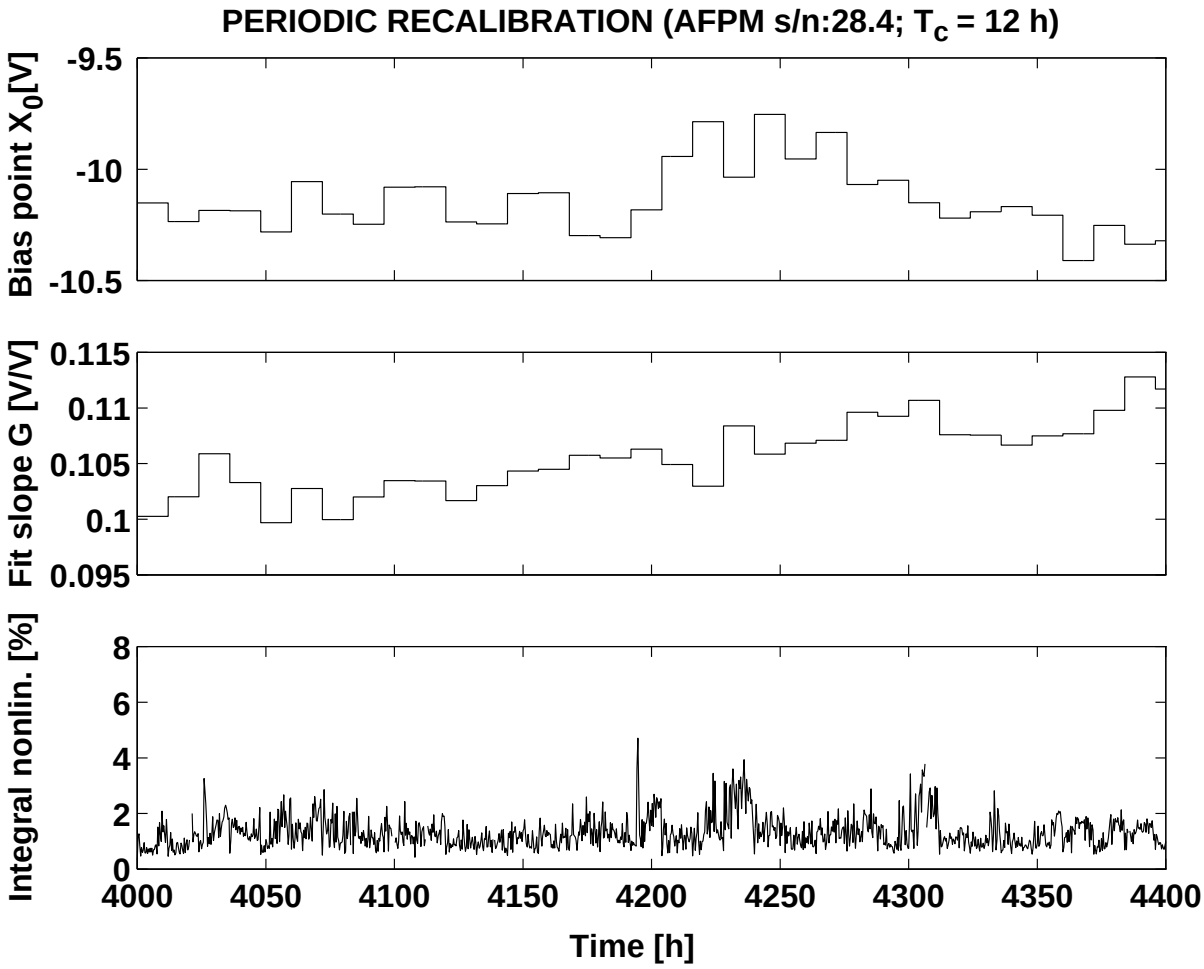

Figure 9: Simulated periodic recalibration (AFPM s.n.28.4). The fit parameters (top and middle graphs) were tuned at discrete time intervals (every T_c = 12 h). The corresponding integral nonlinearity is shown in the bottom graph.

The maximum integral nonlinearity for each interval T_c is retained, and the statistical distribution over all intervals can be plotted as shown in Fig. 10 (T_c = 12 h), giving a quantitative indication of the channel time-stability. To see if the application requirements are satisfied, this plot (and similar ones) are compared to the maximum acceptable error. It can be inferred from Fig. 10 that the integral nonlinearity would not exceed 2.5%, for example, in 75% of the cases.

The previous analysis can be iterated for different T_c to analyse the dependence of the linearity error statistics on the recalibration period. Figure 11 shows the results in the form of compact 'box plots'. The three horizontal lines in the boxes indicate the position of the lower (25%), median (50%), and upper (75%) quartiles; the notches around the median quartiles give an indication of the possible errors due to the limited statistics.

The results of the simulations show that both the average and the distribution around the average of the integral nonlinearity tend to increase as a function of the recalibration period. This confirms expectations. This tendency seems however to saturate towards T_c = 12 h, possibly in correspondence with the daily temperature cycles. Investigation with recalibration periods higher than 12 h did not give significant results because of the limited number of recalibrations performed and the correspondingly poor integral-nonlinearity statistics.

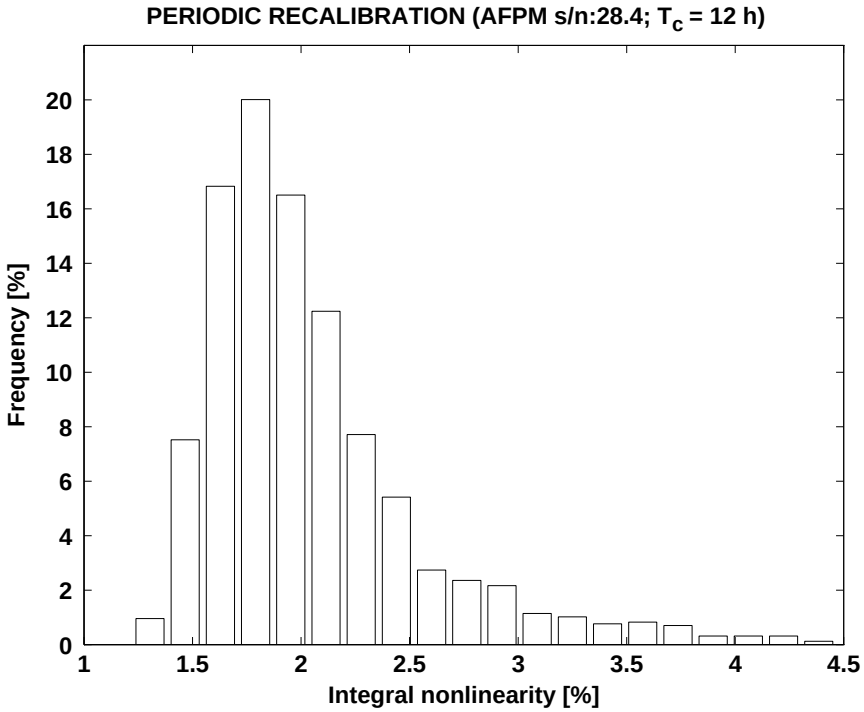

Figure 10: Distribution of the integral-nonlinearity probability for a fixed recalibration period T_c = 12 h (AFPM s.n.28.4).

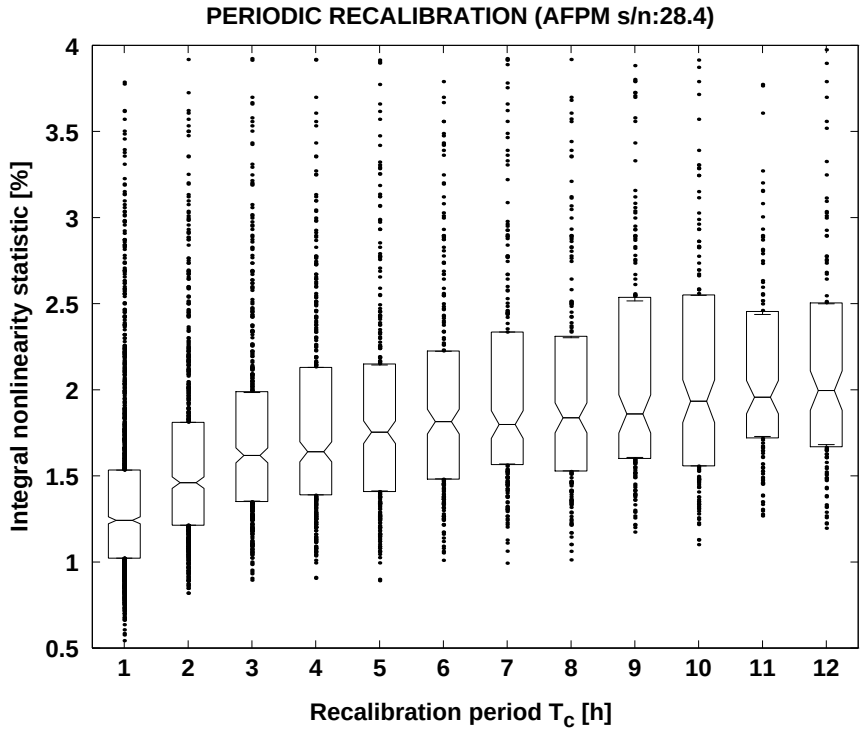

Figure 11: Integral nonlinearity statistics as a function of the recalibration period (AFPM s.n.28.4). The 'box plots' represent the position of the first, second, and third quartiles. The notch around the second quartile gives a visual indication of the estimation reliability.

Based on graphs like the one in Fig. 11, the recalibration period can be optimized (for a given channel) according to the integral-nonlinearity requirements and the corresponding confidence level. Figure 12 shows, for instance, the position of the third quartile as a function of the recalibration period T_c for three of the four tested modulator channels. This indicates the integral nonlinearity which would not be exceeded in 75% of the cases. If the maximum acceptable error, at this confidence level, is for instance α = 2%, we can allow a recalibration period of 1 h for channel s.n.20.4, 3 h for channel s.n.28.4, and more than 12 h for channel s.n.28.3.

This analysis shows that the system performance stability with time can be greatly improved by using a periodic recalibration (compare Figs. 8 and 12). For instance, a periodicity of 6 h would be enough to keep the integral nonlinearity below 3%, with a confidence level of 75%, for all the evaluated channels (see Fig. 12). In general, a compromise has to be made between three parameters: the linear-region width, the maximum acceptable integral nonlinearity, and the recalibration frequency. If the linear-region width is fixed (as in our analysis), then the trade-off is between the maximum integral nonlinearity and the recalibration frequency (as shown in Fig. 12). Alternatively, if the allowed integral nonlinearity is defined, the recalibration period has to be adjusted in order to match the minimum linear-region width requirements.

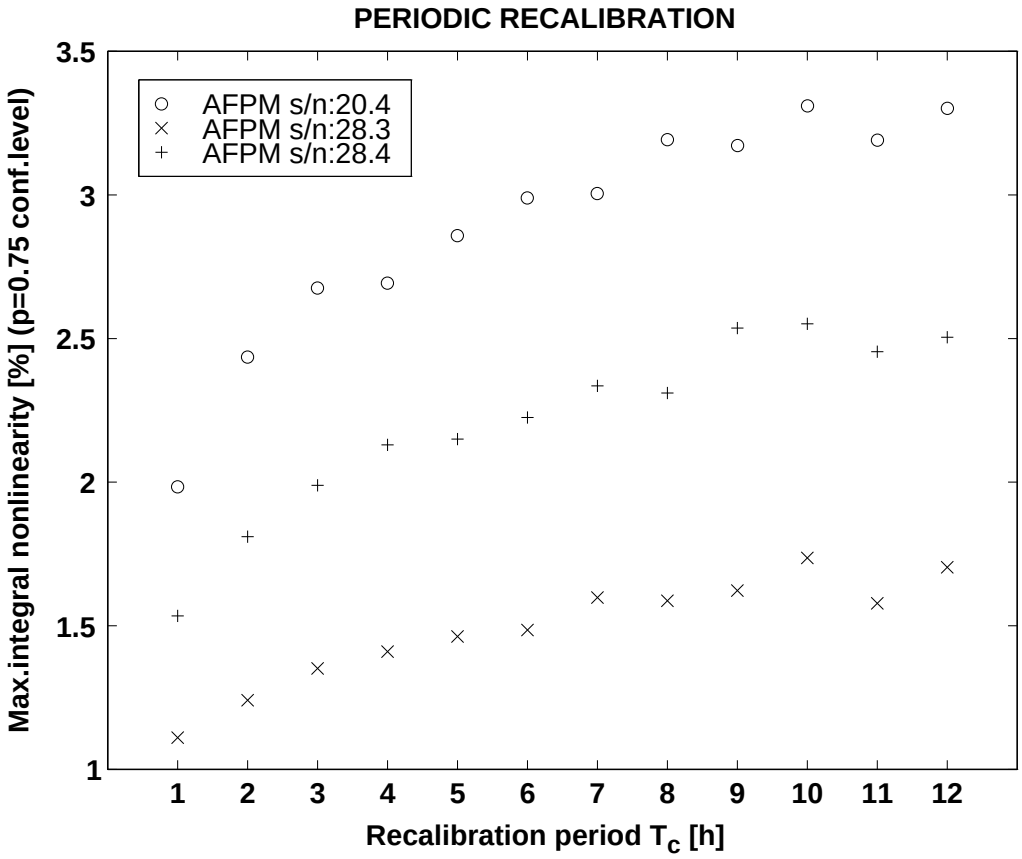

Figure 12: Time-stability performance of the three evaluated channels. The plot represents the third quartile position in the integral-nonlinearity probability distribution as a function of recalibration time. The channel integral nonlinearity is below the plotted value in 75% of all measurements.

6. CONCLUSIONS

Analog AFPM modulator based lightwave links were developed and tested at CERN. A preliminary study of their long-term reliability and stability was carried out. A four-channel link prototype was monitored over a period exceeding 5500 h and a procedure was developed to evaluate its performance as a function of the operational parameters (bias point, linear-fit gain, linear range). The transmitter behaviour, in particular, was shown to be temperature dependent. However in typical LHC applications, the front-end temperature will be stable to within 1°C. Measurements in such a temperature-stabilized environment were recently completed, and results show very stable performance. Nevertheless, periodic recalibration of the operational parameters must be foreseen to maintain optimum performance throughout the whole operational period of the optical link. The integral-nonlinearity statistics were calculated, allowing the system recalibration requirements to be determined. Only a small number of channels were evaluated. Once more channels have been tested, it will be possible to assess average performance levels and define a practical recalibration procedure.

ACKNOWLEDGEMENTS

This work formed part of the DEA thesis of G. Cervelli for the National Polytechnical Institute of Grenoble (INPG), coordinated by Prof. S. Tedjini (ENSERG/LEMO). We gratefully acknowledge Mr. Tedjini's collaboration.

REFERENCES

[1] The CMS Collaboration, The Compact Muon Solenoid technical proposal, CERN LHCC 94–38 (1994).

[2] G. Stefanini, An overview of requirements for optical links in LHC experiments, Proc. First Workshop on Electronics for LHC Experiments, Lisbon, 1995, CERN LHCC 95–56 (1995), pp. 157–159.

[3] F. Vasey, Modulator-based lightwave links for analogue signal transfer at LHC, Proc. First Workshop on Electronics for LHC Experiments, Lisbon, 1995, CERN LHCC 95–56 (1995), pp. 175–179

[4] M.J. Goodwin et al., The application of optoelectronic technologies to high performance electronic processor interconnects, Opt. Quantum Electron. **26**, 455 (1994).

[5] P.J. Duthie et al., Passively aligned 4-channel reflective InP MQW modulator transmitter, Electron. Lett. **31**, 1177 (1995).

[6] Y. Kuhara et al., Reliability of InGaAs/InP long-wavelength p-i-n photodiodes passivated with polymide thin film, J. Lightwave Technol. **4**, 933 (1986).